

Efficient waveguide power combiners at mm-wave frequencies

van Schelven, Ralph ; Spirito, Marco; Cavallo, Daniele

DOI

[10.1049/mia2.12349](https://doi.org/10.1049/mia2.12349)

Publication date

2023

Document Version

Final published version

Published in

IET Microwaves, Antennas and Propagation

Citation (APA)

van Schelven, R., Spirito, M., & Cavallo, D. (2023). Efficient waveguide power combiners at mm-wave frequencies. *IET Microwaves, Antennas and Propagation*, 17(6), 467-477.
<https://doi.org/10.1049/mia2.12349>

Important note

To cite this publication, please use the final published version (if applicable).
Please check the document version above.

Copyright

Other than for strictly personal use, it is not permitted to download, forward or distribute the text or part of it, without the consent of the author(s) and/or copyright holder(s), unless the work is under an open content license such as Creative Commons.

Takedown policy

Please contact us and provide details if you believe this document breaches copyrights.
We will remove access to the work immediately and investigate your claim.

IET Microwaves, Antennas & propagation

Special issue Call for Papers

**Be Seen. Be Cited.
Submit your work to a new
IET special issue**

Connect with researchers and experts in your field and share knowledge.

Be part of the latest research trends, faster.


[Read more](#)



The Institution of
Engineering and Technology

ORIGINAL RESEARCH

Efficient waveguide power combiners at mm-wave frequencies

 Ralph M. van Schelven | Marco Spirito | Daniele Cavallo 

Microelectronics Department, Delft University of Technology, Delft, The Netherlands

Correspondence

 Daniele Cavallo, Microelectronics Department, Delft University of Technology, Delft, The Netherlands.
Email: d.cavallo@tudelft.nl

Funding information

NXP Semiconductors, Grant/Award Number: 15591

Abstract

In this study, an efficient power combiner for mm-wave frequency transmitters is investigated. The combiner is based on a parallel plate waveguide (PPW) excited with multiple parallel feeds. The Doherty power combiner scheme is also integrated in the proposed concept, to increase the efficiency of the amplifiers when implementing amplitude modulation. The advantage of the proposed PPW combiner with respect to other concepts, for example, the ones based on substrate-integrated waveguide, is the wider bandwidth and the scalability to an arbitrary number of inputs. Measured results from a demonstrator realised in standard printed circuit board technology are presented. Two variations of the combiner are implemented, one terminated with a 50 Ω coaxial output, and another integrated with an antenna. In the latter case, the waveguide is folded so that both the power combiner and the antenna fit within a half wavelength size, and thus would be compatible with a dense antenna array implementation.

KEYWORDS

millimetre waves, parallel plate waveguides, power combiners

1 | INTRODUCTION

The fifth generation of mobile communications (5G) has been conceived to meet the growing wireless traffic demands of the coming decade. Challenging requirements on the 5G networks are set to allow for data volume increase, network scalability, and efficient network operation. A key enabler of 5G is the mm-wave frequency range, which can provide large spectrum and consequently high-data rates. This work specifically focuses on the allocated band around 28 GHz.

One of the most challenging aspect of mm-wave communication is related to the efficient generation of radio frequency power. Currently reported mm-wave power amplifiers (PAs) are unable to reach the required output power to account for the loss margins in commercial applications [1, 2]. One typical way to increase the available output power is to combine the signals from multiple PAs using a power combiner. Power combiners in the mm-wave frequency range have been a topic of investigation for many years [3, 4]. Typical solutions are Wilkinson-based combiners [5], but they present area occupancy and losses that grow directly with the number of combined elements. More compact combiners have been proposed [6–8], based on parallel

or series combination, but their operation is restricted by factors such as impedance variation with number of elements, narrow bandwidth and limited impedance transformation. Waveguide-based power combiners were presented in [9–16]. An important advantage of this type of structures, with respect to Wilkinson or transformer based combiners, is that the insertion losses do not increase with the number of feeds, thus resulting in efficient power combiners if a large number of PAs is needed to meet the required output power.

Besides the output power levels, another limitation of mm-wave PAs is the low efficiency [17]. In communication applications, to increase the channel capacity, signal modulations are applied that require the transmitter to deliver a range of output power. By decreasing the output power of the PAs, their operating efficiency is reduced. To overcome this problem, a Doherty power combiner [18] can be implemented, which connects and excites multiple PAs in such a way that the overall operating efficiency of the PAs is maximised for a range of output power. Examples of the implementation of a Doherty power combiner for 5G applications are presented in refs. [19, 20].

In this work, we propose to combine parallel plate waveguide (PPW) power combiner that also includes a Doherty scheme.

This is an open access article under the terms of the Creative Commons Attribution-NonCommercial License, which permits use, distribution and reproduction in any medium, provided the original work is properly cited and is not used for commercial purposes.

© 2023 The Authors. *IET Microwaves, Antennas & Propagation* published by John Wiley & Sons Ltd on behalf of The Institution of Engineering and Technology.

When comparing with rectangular waveguide power combiners presented in [11, 12, 21], the PPW-based solution given here can achieve much wider bandwidth, thanks to the non-dispersive impedance characteristic of the PPW. Moreover, the concept is easily scalable to larger number of inputs, since the impedance of each feed is independent on the number of feeds. A 6-to-1 combiner has been fabricated in standard printed circuit board (PCB) technology and tested. Measured results confirm the low loss and wideband characteristics of the presented concept. A possible integration of the combiner with an antenna operating at around 28 GHz is also proposed and experimentally validated.

2 | PARALLEL PLATE WAVEGUIDE COMBINER

We consider a PPW as shown in Figure 1a. For the transverse electromagnetic (TEM) mode, neglecting fringing fields, the characteristic impedance is given by $Z_{\text{PPW}} = \zeta h/w$, where ζ is the intrinsic impedance of the material filling the PPW, h is the height of the PPW and w is its width. If a delta-gap source is exciting the PPW of semi-infinite length, the input impedance of the source is approximately equal to Z_{PPW} .

If one considers a periodic version of the same geometry (Figure 1b), where an infinite array of PPW fed by delta-gap sources are connected in the transverse dimension, the active input impedance of each source is also approximately equal to $Z_{\text{act}} = \zeta h/w$, where w now refers to the transverse period. Therefore, assuming that no power leaks from the sides of the PPW, that is, the height h is much smaller than the wavelength, the input impedances in both configurations shown in Figure 1 are the same and frequency independent.

To emphasise the non-dispersive properties of PPW combiner, Figure 2 shows a comparison between the active input impedances of a 12-feed power combiner implemented in a substrate-integrated waveguide (SIW) and in a PPW, over the frequency range of interest. The height of the structure is $h = 100 \mu\text{m}$ and the width of the sections is $w = 400 \mu\text{m}$, also equal to the centre-to-centre distance between feeds. The waveguides are filled with a dielectric with relative permittivity $\epsilon_r = 3.66$, such that the characteristic impedance is $Z_{\text{PPW}} = 50 \Omega$. The feeds are all excited with equal amplitude and phase. Due to the symmetric nature of the structures, only the active impedance of 6 ports are shown. It is clear from Figure 2 that the active input impedance seen from the

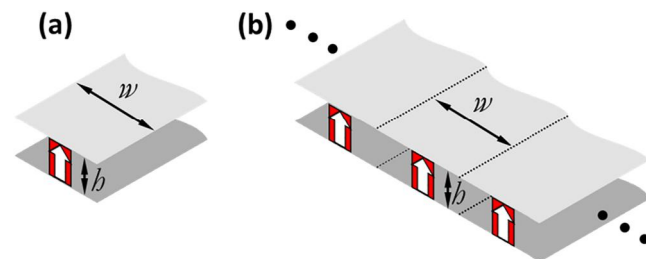


FIGURE 1 (a) Single parallel plate waveguide (PPW) fed with a lumped port depicted as a red rectangle and (b) multiple connected PPWs in parallel.

different ports inside the SIW is not only frequency dependent, but also largely varying from port to port. On the contrary, the active impedances for the PPW are nearly constant with frequency and show very little variation between the different ports.

It can be expected that, in the SIW case, providing different weights to the feeds according to the sinusoidal distribution of the fundamental TE_{10} mode would improve the impedance variability, but this is not practical. Moreover, although individual SIWs fed by a single PA and then combined in pairs by means of T-junctions would give a stable impedance at all the inputs, they would also result in a much larger structure: each of the 12 SIWs has to be wider than half wavelength ($\approx 3.5 \text{ mm}$) for the TE_{10} mode to propagate, while the entire combiner considered in Figure 2 is 4.8 mm wide.

3 | PPW PARALLEL DOHERTY COMBINER

In this section we propose a concept that combines the PPW parallel combiner with the Doherty scheme. The Doherty combiner [18] provides a matching network, which aims at maximising the efficiency of the PAs over a range of output power. The circuit model is shown Figure 3a, which represents a two-way series Doherty combiner [20]. This consists of two PAs, one referred as ‘main’ and the other as ‘peaking’, connected by a quarter-wave transmission line with characteristic impedance Z_0 . The output load is indicated as Z_l and can represent, for instance, a waveguide or a radiating structure. The two PAs are assumed to be identical and can be represented as equivalent, voltage controlled, Norton current sources, as described in Appendix. By tuning the control signal

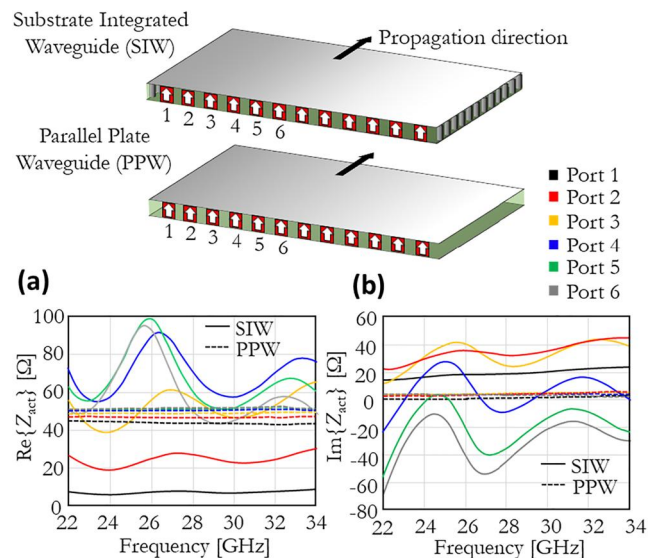


FIGURE 2 Comparison of active (a) input resistance and (b) input reactance seen from 12 ports feeding a parallel plate waveguide (PPW) (dashed) and a substrate-integrated waveguide (SIW) (solid). Because of symmetry, only the impedances of 6 feeds are shown.

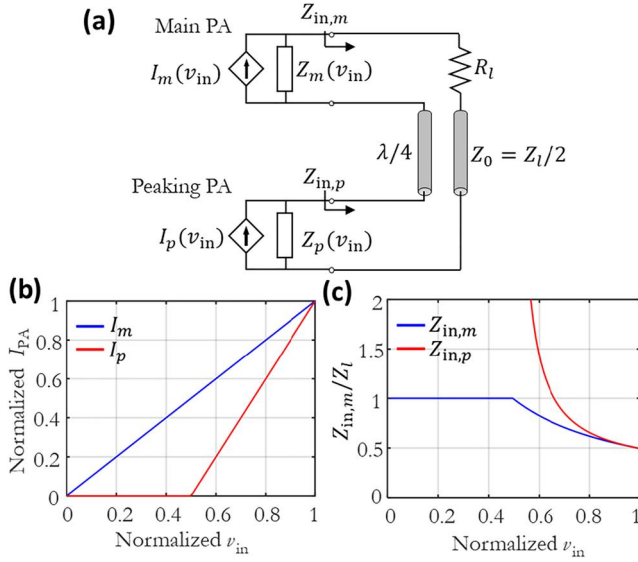


FIGURE 3 (a) Circuit representation of a two-way series Doherty combiner, (b) normalised generator current and (c) input impedance of an ideal combiner as seen from the main power amplifier (PA) and the peaking PA as a function of v_{in} .

v_{in} , both the current and the impedance of the Norton sources vary, to provide a desired level input power.

To implement the Doherty scheme, the values of the equivalent generator currents for the main and peaking PAs, I_m and I_p , depend on v_{in} as follows

$$I_m(v_{in}) = v_{in}/Z_{norm} \quad (1)$$

$$I_p(v_{in}) = \begin{cases} j(2v_{in} - 1)/Z_{norm} & \text{for } v_{in} \geq 0.5 \\ 0 & \text{otherwise} \end{cases} \quad (2)$$

where Z_{norm} is a frequency-dependent normalisation impedance, which depends on the maximum value of v_{in} that satisfies the condition (A4). The generator currents are plotted in Figure 3b as a function of v_{in} . Following the steps as described in ref. [26], it is found that the characteristic impedance of the quarter-wave section must satisfy the condition $Z_0 = Z_l/2$. The normalised input impedance, as seen from the main PA and the peaking PA, of an ideal combiner as a function of v_{in} , is shown in Figure 3c. It can be seen that the input impedance of the main PA is constant $Z_{in,m} = Z_l$ until $v_{in} = 0.5$ (referred to as power back-off), after which it decreases to half its original value $Z_{in,m} = Z_l/2$. The input impedance of the peaking PA starts from infinity at power back-off and drops to $Z_{in,p} = Z_l/2$ for $v_{in} = 1$ (full power).

A PPW implementation of the two-way Doherty combiner is shown in Figure 4a. The PPW consists of two sections, one quarter-wave long between the main PA and the peaking PA, with height b_1 , and another representing the output waveguide, with height b_2 and characteristic impedance equal to Z_l . The heights of the two sections are related by $b_1 = b_2/2$, so that the characteristic impedance of the quarter wave section is $Z_0 = Z_l/2$. The PAs are represented as delta-gap sources

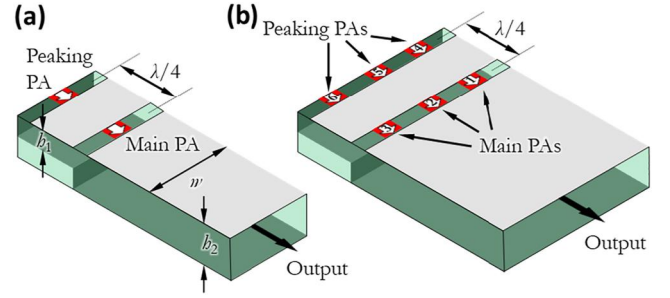


FIGURE 4 Parallel plate waveguide (PPW) implementation of a Doherty power combiner, for (a) a single main and peaking power amplifier (PA) and (b) multiple main and peaking PAs in parallel.

located in slots etched on the top metal plate of the PPW. Similar to the structure described in Section 2, multiple feeds can be placed in each slot as in Figure 4b, without significantly altering the input impedances seen by the feeds. The width of the PPW increases with number of parallel feeds N and the characteristic impedance of the entire PPW decreases accordingly as Z_l/N , but can be tapered to a higher impedance and be connected, for instance, to a radiating structure. As an example, the PPW Doherty combiner with three main and three peaking PAs is considered. The PPW is filled with a material with $\epsilon_r = 3.66$. The width of the three PPW sections is $w = 750 \mu\text{m}$, $b_1 = 101 \mu\text{m}$ and $b_2 = 202 \mu\text{m}$. The characteristic impedances of the two waveguide sections are $Z_0 = 25 \Omega$ and $Z_l = 50 \Omega$.

4 | SIMULATION RESULTS

The structure is simulated in CST and the S-parameters are combined in post-processing to calculate the active impedances and the efficiency. The inputs representing the main PAs are numbered 1, 2, and 3, while the peaking PAs are numbered 4, 5, and 6. Figure 5a shows the active impedances seen from the main PAs at power back-off, for which ports 1, 2, and 3 are active, while ports 4, 5, and 6 are switched off. The passive ports are assumed to be terminated on a load $Z_p = 480 \Omega$, which represents the parasitics of the PA when it is inactive, as described in Appendix. The figure also shows the generator impedance Z_m , as a function of frequency. It can be seen that the value of the generator impedance Z_m differs from the ideal value of 50Ω and varies as a function of the frequency, to satisfy the condition (A4). The stepped nature of the generator impedance curve is due to the assumption that the PA is composed of a finite number of sub-PAs, that are either on or off (see Appendix), resulting in a quantised characteristic.

Similarly, the active input impedances and the generator impedances at full power, when all 6 ports are active, are shown in Figure 5b. In this case, the input impedances and the generator impedances are seen to be approximately equal to half of their values for the power back-off case, as expected.

The efficiency of the combiner is found as the ratio between the output power, P_{out} and the supply power P_{supply} , as

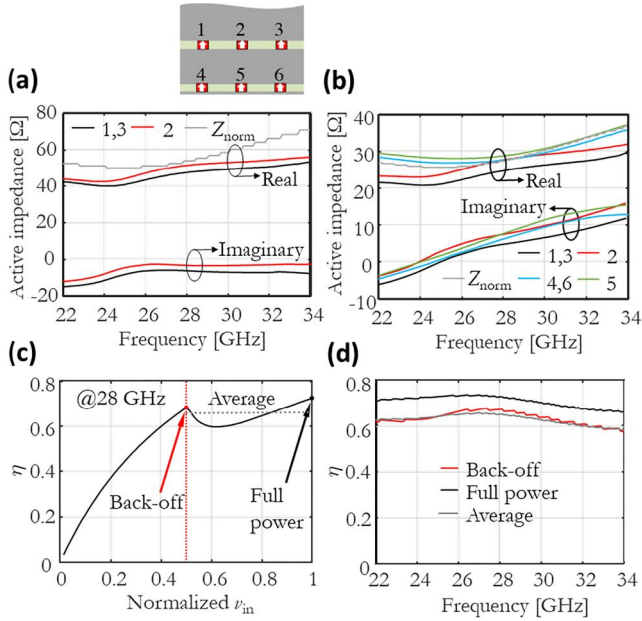


FIGURE 5 Active impedance seen from the six power amplifiers (PAs) in the parallel plate waveguide (PPW) Doherty combiner (a) at power back-off and (b) at full power. Efficiency of the PPW Doherty combiner (c) for increasing v_{in} at 28 GHz and (d) as a function of frequency. The efficiency is shown at power back-off, at full power and the average efficiency between back-off and full power.

defined in Appendix. Figure 5c shows the efficiency of the combiner at 28 GHz as a function of the normalised input voltage v_{in} . The characteristic efficiency curve of a Doherty combiner can be observed, with peaks both at power back-off and at full power. The efficiency as a function of frequency is presented in Figure 5d. Three curves are shown: the efficiency at power back-off, the efficiency at full power and the average efficiency between these two points. It can be seen that, over the entire frequency range of interest, all three curves are higher than 60%. Note that the maximum theoretical efficiency is 79% from Equation (A3).

5 | PCB DEMONSTRATOR AND MEASURED RESULTS

To validate the concept described in the previous section, a demonstrator is fabricated in standard PCB technology. A 6-to-1 PPW Doherty combiner is designed, where the transition from the PPW with characteristic impedance $Z_l = 50/3 \approx 17 \Omega$ to a 50Ω microstrip output is realised using a tapered impedance transformer of length l_{taper} , as shown in Figure 6a.

A section with length l_{PPW} of straight PPW separates the feeding slots from the taper, to ensure that the desired TEM mode is formed before entering the PPW taper. Comparing Figure 6a with Figure 4b, it can be seen that the feeding slots have been placed on the side of the PPW with the electric field oriented vertically. This allows placing the feeding lines in the same metal layers as the top and bottom plates of the PPW, making the routing of the feeding microstrip lines more

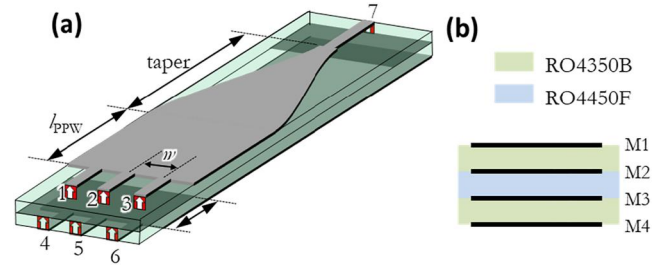


FIGURE 6 (a) Design of the 6-to-1 parallel plate waveguide (PPW) Doherty combiner with a tapered impedance transformer from the PPW to the output microstrip; (b) schematic sideview of the printed circuit board (PCB) stack-up.

convenient. Figure 6b shows the schematic side view of the PCB stack-up. Four metal layers are considered, printed on Rogers RO4350 B dielectric slabs ($\epsilon_r = 3.66$, $\tan \delta = 0.0037$ at 10 GHz) with a height of $101 \mu\text{m}$. The two slabs are then bonded together using Rogers RO4450 F bondply ($\epsilon_r = 3.52$, $\tan \delta = 0.004$ at 10 GHz), of the same height.

The geometrical parameters of the design are $b_1 = 101 \mu\text{m}$, $b_2 = 202 \mu\text{m}$, $w = 750 \mu\text{m}$, $l_{PPW} = 1.4 \text{ mm}$ and $l_{taper} = 5.6 \text{ mm}$. The width of the microstrip feeding lines is $w_{line} = 200 \mu\text{m}$, with characteristic impedance of 50Ω . The lines extend a few centimetres to reach top mounted 50Ω Rosenberger 02K722-40MS3 solderless connectors. Figure 7 shows the fabricated demonstrator. It can be seen from Figure 7a that Through-Reflect-Line (TRL) calibration lines are also present on the board, to de-embed the effect of the connectors and the different feeding lines, placing the reference plane of the measurements at the location where the microstrips feed the PPW (Figure 7d). All the 7-port S-parameters have been measured, with the passive ports terminated on 50Ω loads. Also the error boxes of the feeding lines have been characterised by measuring the TRL structures. When de-embedding the error boxes, the results in Figure 8 are obtained for the passive reflection coefficients at the input ports. It can be seen that the measured curves oscillate around the simulated ones for most cases. Nevertheless, a problem with port 5 is observed, that is, the measured curve in Figure 8d shows a clear resonance around 29 GHz that is not present in the simulation. Large oscillations of the measured S_{15} with respect to simulations are also observed.

To investigate the causes of this discrepancy, we apply the inverse Fourier transform of the S-parameters S_{ii} for $i = (4; 5; 6)$ and plot the time-domain signals associated with the ports 4, 5 and 6 in Figure 9a, as a function of the distance from the cable tip. From this analysis we observed that ports 4 and 6 only exhibit a main reflection at the end of the feeding line, as expected. On the contrary, S_{55} shows an additional unexpected reflection at a distance indicated by X, which corresponds to the region where the line of port 5 (line 5) runs underneath the connector of port 2 (see Figure 9b). In this region several plated through hole vias are present, which causes a sinking effect of the microstrip line locally around the vias, as shown in Figure 10. The prepreg tends to fill the via holes, so that the microstrip line locally drops closer to the ground plane, yielding a variation of

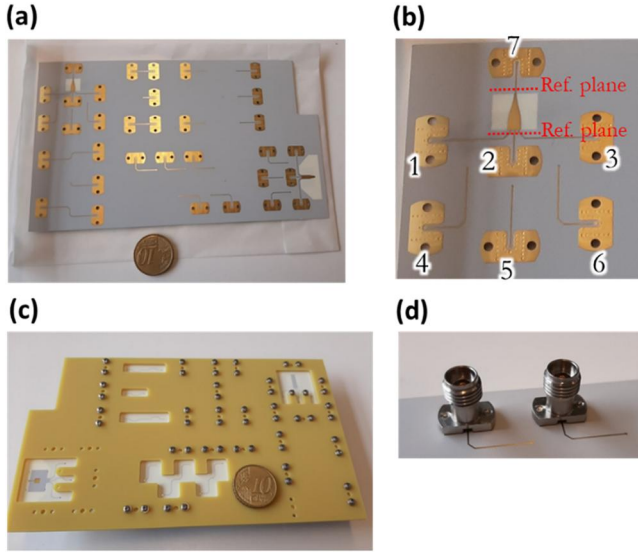


FIGURE 7 Photographs of the fabricated demonstrator: (a) entire board with demonstrator and TRL-calibration lines, (b) zoom of the 6-to-1 parallel plate waveguide (PPW) Doherty combiner with port numbering and reference planes; (c) back view of the assembled demonstrator board; (d) top mounted coaxial connectors.

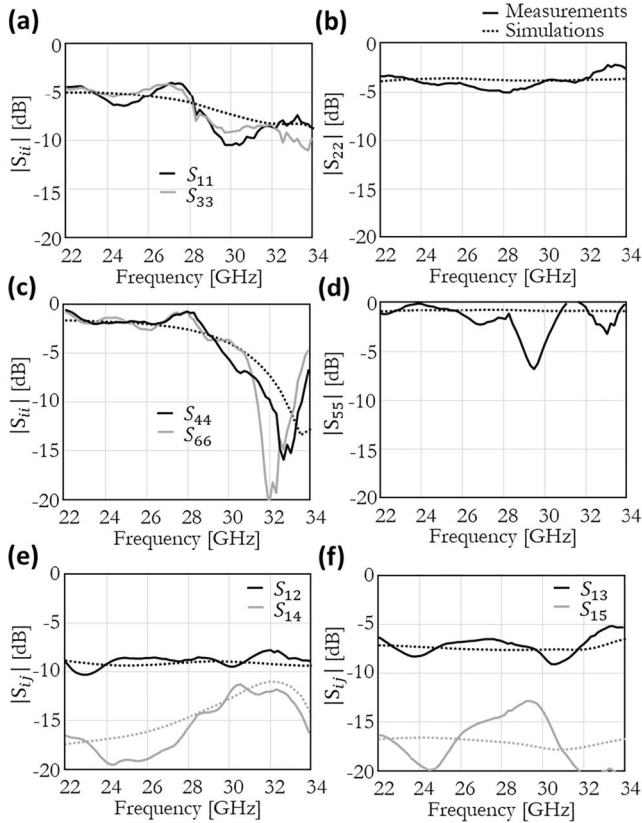


FIGURE 8 Comparison between simulated and measured reflection coefficients after de-embedding: (a) S_{11} and S_{33} , (b) S_{22} , (c) S_{44} and S_{66} , (d) S_{55} , (e) S_{12} and S_{14} , (f) S_{13} and S_{15} .

the characteristic impedance. This phenomenon occurs in the device under test, but not in TRL structure, where the vias are not present. To confirm the given explanation, we simulated the

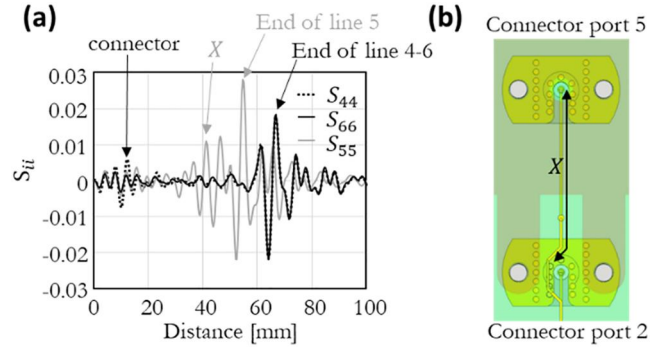


FIGURE 9 Time domain analysis for S_{44} , S_{55} and S_{66} . Several expected reflections are indicated, as well as an unexpected reflection. (b) Routing of line 5 to go underneath the vias of connector 2.

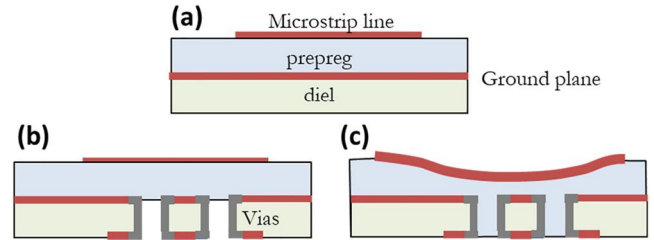


FIGURE 10 Effect of routing a microstrip line over vias in the ground plane: (a) microstrip line as designed; (b) metal plated vias are introduced beneath the line; (c) during the bonding process the melted prepreg thins down by filling the via holes, changing the characteristic impedance of the line.

structure with a microstrip line locally sunk by $60\ \mu\text{m}$ and the simulated results reproduce better the measured ones, as shown in Figure 11, for both the total structure and after de-embedding. In the remainder of the section, we then consider the simulated line 5 for the de-embedding of the error box, instead of the TRL measurements. While this approach improves the quality of the results for the device under test, the hybrid de-embedding procedure causes some residual inaccuracy in calibrating out the error boxes.

The reflection coefficients in Figure 8 are relative high, because they refer to passive parameters. Instead, the structure is designed to be matched in terms of active reflection coefficients, that is, when all ports are simultaneously excited. In this section, the input ports are combined by a post-processing procedure, according to the Doherty combining scheme [18]. Figures 12a,b show the active impedance of the different ports as a function of the frequency at back-off and at full power respectively. It can be seen that the active impedances of ports 1, 2, and 3 at back-off are oscillate around $50\ \Omega$, while at full power the active impedances fluctuate around $25\ \Omega$. The effect of the oscillations of the impedances compared to the ideal values can be quantified by investigating the PA efficiency as a function of frequency in Figure 12c. Three curves are shown: the PA efficiency at back-off, at full power and the average value between these two points. The measured efficiency is slightly lower than the simulated one, mainly due to residual mismatch of the error boxes. However, within the frequency

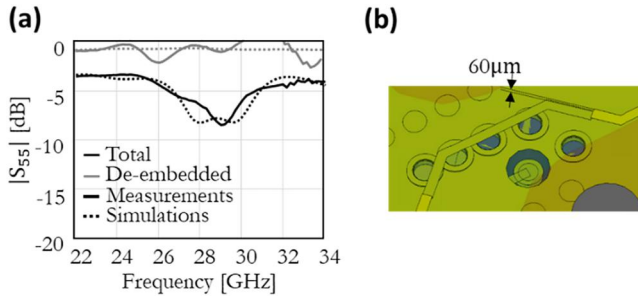


FIGURE 11 (a) Comparison between measured and simulated S_{55} with error boxes included and after de-embedding, where the error box of line 5 is simulated considering (b) a sunk region of the microstrip around the vias.

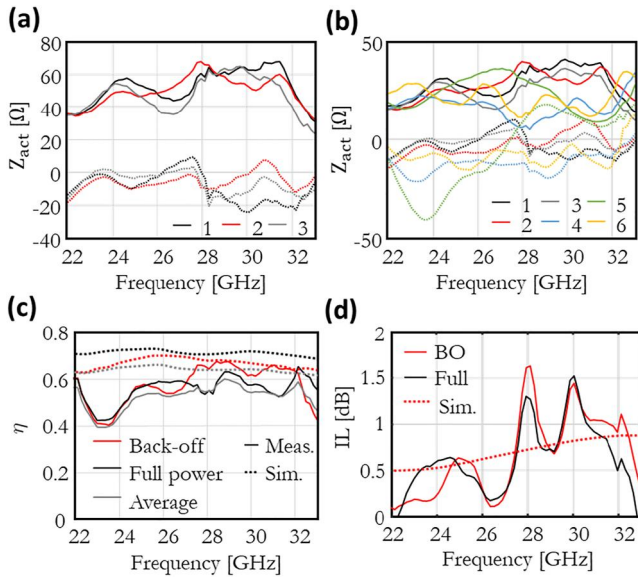


FIGURE 12 Active impedance seen from the power amplifiers (PAs) (a) at back-off and (b) at full power; (c) comparison between PA efficiency at back-off, full power and the average value, calculated from the simulated and measured structure; (d) (b) Measured insertion losses of the combiner at back-off and at full power.

band from 24 to 32 GHz all three curves of the PA efficiency are higher than 50% and oscillating around 60%, confirming the wideband characteristic of the combiner. The IL due to Ohmic losses and radiation of the structure can be estimated as

$$\Pi_{\text{dB}} = -10 \log_{10} \sum_{i=1}^7 |S_{i7}|^2. \quad (3)$$

A comparison between the simulated and measured IL is shown in Figure 12d. The measured loss oscillates around the simulated value. Again, these fluctuations are consistent with the non-ideality of the TRL calibration. It can be noted that the insertion losses for the two excitation cases are approximately equal, thus they do not increase when doubling the number of feeds from three to six.

6 | INTEGRATION WITH ANTENNA

This section describes the integration of the PPW Doherty combiner with an antenna. A PCB demonstrator is fabricated and measurements are presented. An advantage of the proposed combiner is the convenient integration with a radiating element. In Section 4 the PPW was ended in a 50Ω microstrip output. In this section, the combiner is directly connected to an antenna. A conceptual drawing of the combiner-antenna co-design is shown in Figure 13a. A chip with the PAs can be connected in a flipped chip configuration to the PCB, so that the PAs excite the PPW. The waveguide has a tapered bottom plate, similar to the previous design, is folded over its top plate through a via and is connected to a patch antenna. The top plate of the waveguide now also serves as a backing reflector for the patch antenna. A matching layer is added above the patch as superstrate, realised using artificial dielectric layers (ADLs) [23, 24]. By folding the waveguide, the total size of the structure can be reduced to fit within a half wavelength unit cell making it suitable to be used in a phased array.

In this paper, we demonstrate the combiner-to-antenna transition, while the integration with the chip will be the scope of a future work. The 6-to-1 combiner with the antenna are designed with the same layer stack-up as the combiner alone. The PPW Doherty combiner until the taper is identical to the design depicted in Figure 6. The plate on M1 is tapered to a smaller width and is connected through a via to M4, where the patch antenna is printed (see Figure 13b). The total size of the patch antenna is 2.1×2.1 mm, to resonate around 28 GHz. Because of the very close proximity of the patch antenna to the backing reflector, a three layer ADL superstrate is added as a matching layer [25]. The ADL superstrate enhances the front-to-back ratio of the antenna, therefore improving the impedance matching. The ADLs are also fabricated in the same layer stack-up, cut out and glued to the board on top of the antenna (see Figure 13c). The dimensions of the ADL, as depicted in the inset of Figure 13a, are $p = 1.2$ mm, $w = 0.3$ mm and $s = 0.35p$, so that the effective relative permittivity of the ADL for normal incidence is $\epsilon_r = 70$. The patch antenna is matched to 25Ω , allowing for a shorter tapered section transforming from 17 to 25Ω , rather than to 50Ω as for the combiner with coaxial output. The 6-to-1 combiner with antenna is simulated in CST and the active S-parameters are considered both at back-off ($Z_m = 50 \Omega$, $Z_p = 480 \Omega$) and at full power ($Z_m = Z_p = 25 \Omega$). The antenna impedance is presented in Figure 14a and the resulting S-parameters of the combiner terminated with the antenna are shown in Figures 14b,c. It can be seen that the total structure is well matched ($S_{\text{act}} < -10$ dB) over about a 2 GHz bandwidth centred at 28 GHz. Although wider bandwidth could be achieved by increasing the distance between the patch antenna and the backing reflector, the scope of this prototype is to demonstrate the combiner-antenna transition more than to maximise the bandwidth. Figure 14d shows the simulated operating efficiency at back-off, full power and the average efficiency between these two points for the combiner integrated with the antenna. It can be seen that all three curves are

higher than 0.5 within the antenna matching bandwidth. The small peaks in the efficiency curves come from the way the PA is modelled, as described in Appendix A: the number of sub-PAs that are active is varied to verify the condition in Equation (A4), resulting in a discontinuous behaviour of the efficiency curves, especially in the frequency range when higher mismatch occurs.

The fabricated demonstrator of the 6-to-1 combiner with antenna is shown in Figure 15. The feeding network is identical to one used for the combiner without antenna in Section 4.

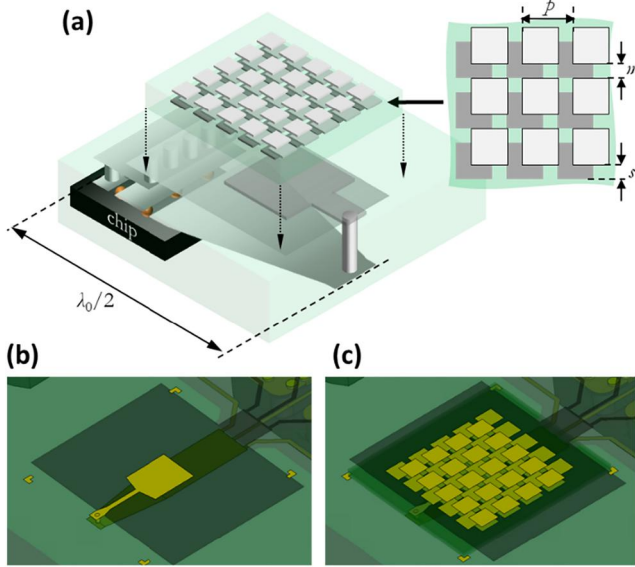


FIGURE 13 (a) Concept of combiner integrated with antenna within a half wavelength unit cell, with artificial dielectric layers (ADLs) added for impedance matching; (b) designed 6-to-1 combiner with antenna and (c) same structure with artificial dielectric superstrate.

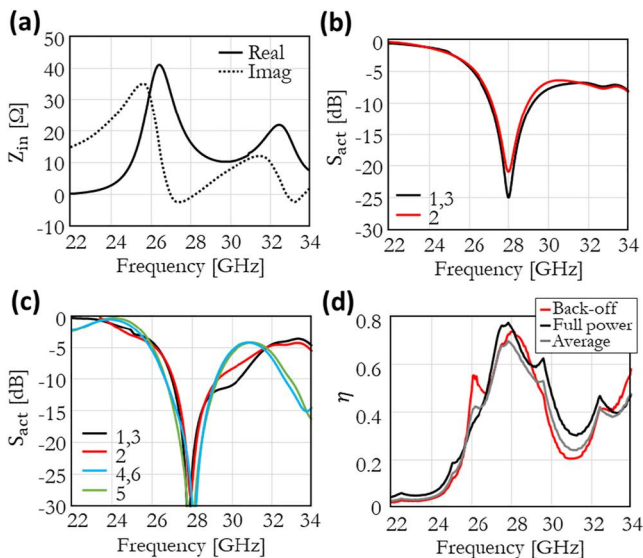


FIGURE 14 (a) Input impedance of the patch antenna with artificial dielectric layer (ADL) superstrate; Active S-parameters of the combiner with antenna: (b) back-off, (c) full power; (d) Operating efficiency of the power amplifiers (PAs), calculated as described in Section 3.

Figure 16 shows the comparison between several measured and simulated S-parameters of the total structure, including the feeding lines and the connectors. It can be seen that most measured curves follow a similar trend as the simulated ones. Similar comparison was observed for ports 4, 5, and 6, not shown here for the sake of brevity. It can be seen that, while all the simulated values are slightly higher than the measured ones, S_{22} shows a different behaviour, as well as an unexpected dip at 33 GHz. This discrepancy is also visible in the phases of the S-parameters, as shown in Figure 17. A good agreement can be seen for most curves, however there is a phase difference between the simulated and measured values for the S-parameters involving port 2. By applying an inverse Fourier

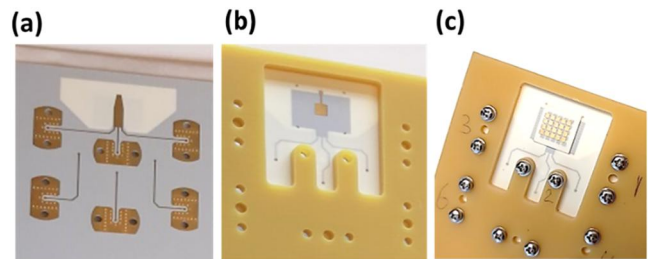


FIGURE 15 Fabricated 6-to-1 combiner with antenna. (a) Back. (b) Front without connectors and artificial dielectric layer (ADL). (c) Front with connectors and ADL attached.

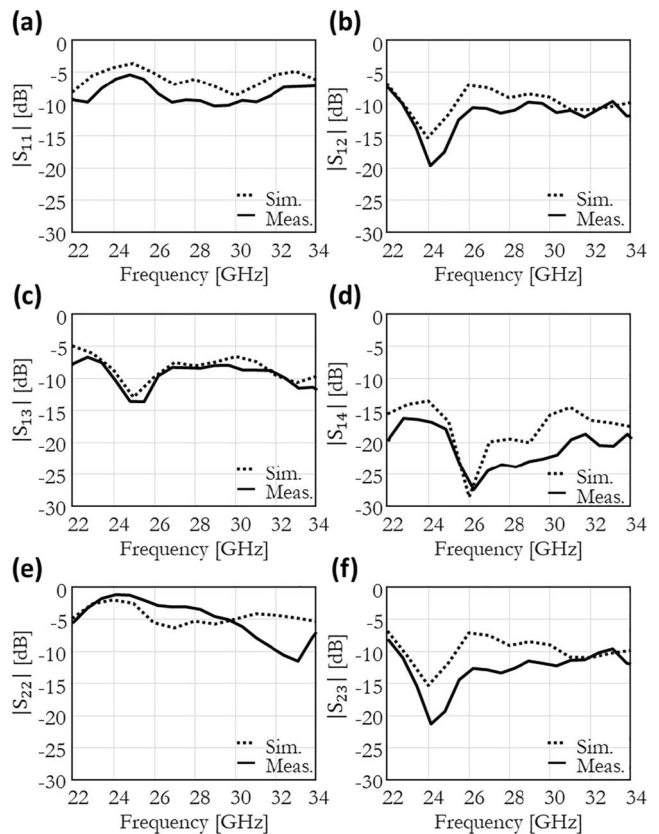


FIGURE 16 Comparison between simulated and measured amplitude of (a) S_{11} , (b) S_{12} , (c) S_{13} , (d) S_{14} , (e) S_{22} , and (f) S_{23} .

transform on the spectrum of the S-parameters, a time-domain analysis is performed. Figure 18 shows the time-domain reflection coefficient of ports 1, 2, and 3 for the combiner without antenna (Section 4) and with antenna. In both figures, clear reflections can be seen at the end of the feeding lines, as expected. However, it can be seen that an extra reflection occurs for port 2, at a distance that corresponds to the connector. This problem appears to be due to a local compression of the PCB after screwing the solderless connectors multiple times.

The measured radiation pattern of the antenna is presented in Figures 19a,b, compared with simulations, for both E- and

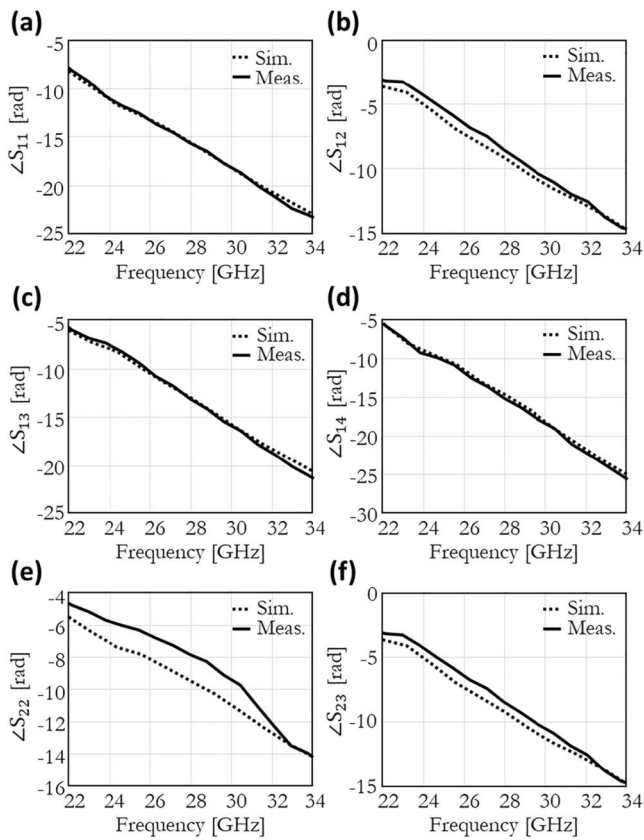


FIGURE 17 Comparison between simulated and measured phase of (a) S_{11} , (b) S_{12} , (c) S_{13} , (d) S_{14} , (e) S_{22} , and (f) S_{23} .

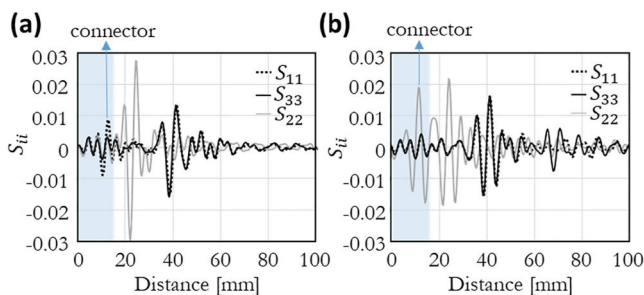


FIGURE 18 Time domain representation of the measured values of S_{11} , S_{22} and S_{33} for (a) the structure with the tapered impedance transformer from Section 4, and (b) the structure with the antenna.

H-plane at 28 GHz. Both co- and cross polarisation show a good comparison. Higher differences are observed at very wide angles, especially in the H-plane. These are due to the absorbers placed beside the antenna to shield the edges of the support structure, as schematically shown in Figure 19c.

Figure 20 shows a comparison between gain and directivity of the structure when port 1 is excited. Measured results are compared with simulation from CST Studio Suite. The measured value for the directivity is calculated by estimating the radiated power from a linear interpolation between the two principal planes. For the simulated gain, a range is presented between an upper bound, corresponding to surface roughness equal to $0.4 \mu\text{m}$, and a lower bound referring to a root mean square roughness of $2.8 \mu\text{m}$, as specified in ref. [27]. The measured gain is observed to mostly fall within this range. It is important to note that, in the region of maximum gain around 27 GHz, the difference between directivity and gain is approximately 5 dB in both simulations and measurements. This value includes the effect of the feeding lines. Simulations of the structure without the feeding lines shows that about 1 dB total losses are associated with the power combiner and the antenna.

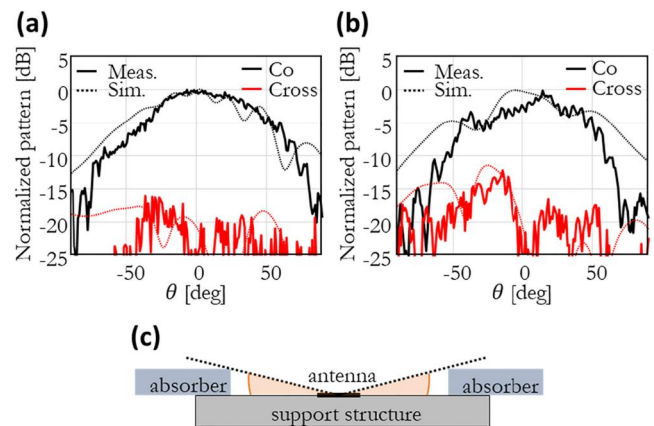


FIGURE 19 Comparison between measurements and CST of the normalised (a) E-plane and (b) H-plane patterns, at 28 GHz; (c) Schematic drawing of measurement setup, explaining lower values for high angles.

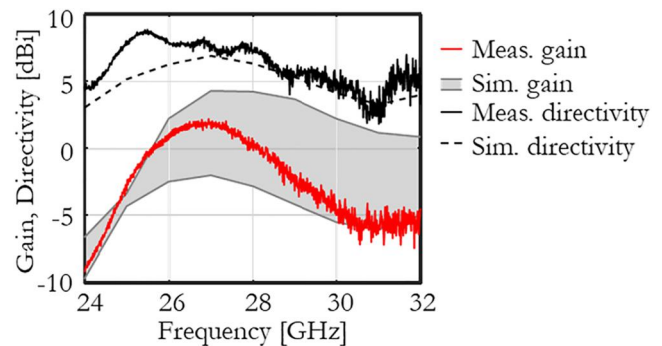


FIGURE 20 Comparison between simulation and measurement of gain and directivity.

7 | CONCLUSION

We presented an efficient and wideband power combiner based on a PPW structure. The proposed design is meant to combine signals from multiple PAs operating in the 28 GHz band for increased output power. The PPW is excited at several locations periodically spaced in the transverse dimension. The active impedances of the ports were shown to be very similar between the different ports and constant with frequency, allowing for wideband operation. A Doherty combiner scheme was also implemented in the PPW combiner, so that two sets of feeding points, representing main and peaking sources, can support a higher operating efficiency of the PAs over a range of output power. Based on the required power, the number of inputs connected in parallel can be easily changed. A 6-to-1 combiner was fabricated in standard PCB technology and measurement results were presented, showing good agreements with simulated results. The efficiency of the structure, accounting for both operating efficiency of the PAs and the impedance mismatch of the combiner, was found to be around 60% over a large bandwidth, from 24 to 32 GHz that includes several relevant 5G bands for mm-wave communication.

A design of the 6-to-1 Doherty combiner integrated with an antenna was also presented. The measured S-parameters of the total structure show a good agreement with the simulations. Also, the radiation characteristics of the antenna compare well with the expected values from simulations. The waveguide folds over itself to reduce the size of the antenna + combiner to fit within $0.5\lambda \times 0.5\lambda$, making it suitable for possible array implementations.

AUTHOR CONTRIBUTIONS

Ralph M. van Schelven: Formal analysis; Investigation; Methodology; Validation, Writing—original draft. **Marco Spirito:** Funding acquisition; Project administration; Supervision; Writing—review & editing. **Daniele Cavallo:** Conceptualisation; Investigation; Supervision, Writing—original draft.

ACKNOWLEDGEMENTS

Dutch Technology Foundation NWO-TTW (WAtt LEvel transmitters at mmwaves (WhALE, project no. 15591)), as part of the TTW-NXP partnership programme “Advanced 5G Solutions”.

CONFLICT OF INTEREST STATEMENT

The authors declare no conflicts of interest.

DATA AVAILABILITY STATEMENT

The data that support the findings of this study are available from the corresponding author upon reasonable request.

ORCID

Daniele Cavallo  <https://orcid.org/0000-0003-1514-3656>

REFERENCES

1. Shan, H., et al.: Implementation of a differential mm-wave CMOS SOI power amplifier. In: IEEE MTT-S Int. Microw. Symp. Hardware Systems 5G and beyond, pp. 1–3 (2019). <https://doi.org/10.1109/IMC-5G47857.2019.9160371>
2. Motaseri, M.H., et al.: Design of stacked-MOS transistor mm-wave class C amplifiers for Doherty power amplifiers. In: IEEE Nordic Circuits Systems Conf, pp. 1–5. Tallinn (2018). <https://doi.org/10.1109/NORCHIP.2018.8573519>
3. Chang, K., Sun, C.: Millimeter-wave power-combining techniques. IEEE Trans. Microwave Theor. Tech. 31(2), 91–107 (1983). <https://doi.org/10.1109/TMIT.1983.1131443>
4. Hwu, R.J., et al.: Array concepts for solid-state and vacuum microelectronics millimeter-wave generation. IEEE Trans. Electron. Devices. 36(11), 2645–2650 (1989). <https://doi.org/10.1109/16.43767>
5. Kim, J.-G., Rebeiz, G.M.: Miniature four-way and two-way 24 GHz Wilkinson power dividers in 0.13 um CMOS. IEEE Microw. Wireless Compon. Lett. 17(9), 658–660 (2007). <https://doi.org/10.1109/LMWC.2007.903451>
6. Zhao, Y., Long, J.R., Spirito, M.: Compact transformer power combiner for millimeter-wave wireless applications. In: IEEE Radio Frequency Integrated Circuits Symposium, pp. 223–226. Anaheim (2010). <https://doi.org/10.1109/RFIC.2010.5477373>
7. Long, J.R., et al.: Silicon VLSI catches the millimeter wave. IEEE Commun. Mag. 49(10), 182–189 (2011). <https://doi.org/10.1109/MCOM.2011.6035834>
8. Long, J.R., et al.: Passive circuit technologies for mm-wave wireless systems on silicon. IEEE Trans. Circuits Syst. 59(8), 1680–1693 (2012). <https://doi.org/10.1109/TCSI.2012.2206499>
9. Sun, H., et al.: Mm-wave waveguide traveling wave power combiner design using an equivalent circuit model. IEEE Access 7, 88327–88337 (2019). <https://doi.org/10.1109/ACCESS.2019.2925897>
10. Cheng, N.S., et al.: 20 watt spatial power combiner in waveguide. IEEE Mtt-s Int. Microw. Symp. Dig. 3, 1457–1460 (1998). <https://doi.org/10.1109/MWSYM.1998.700649>
11. Hu, Z., et al.: Integrated waveguide power combiners with artificial dielectrics for mm-wave systems. IEEE Int. Microw. Symp, 646–649 (2017). <https://doi.org/10.1109/MWSYM.2017.8058652>
12. Roev, A., et al.: Wideband mm-Wave transition between a coupled microstrip line array and SIW for highpower generation MMICs. IEEE Microw. Wireless Components Lett. 28(10), 867–869 (2018). <https://doi.org/10.1109/LMWC.2018.2864869>
13. Eccleston, K.W., Sun, Q.-C., Yeo, S.P.: Tapered microstrip line power combiners with colinear input ports. Microw. Opt. Technol. Lett. 15(6), 339–342 (1997). [https://doi.org/10.1002/\(sici\)1098-2760\(19970820\)15:6<339::aid-mop1>3.0.co;2-f](https://doi.org/10.1002/(sici)1098-2760(19970820)15:6<339::aid-mop1>3.0.co;2-f)
14. Li, L., Wu, K.: Integrated planar spatial power combiner. IEEE Trans. Microw. Theor. Tech. 54(4), 1470–1476 (2006). <https://doi.org/10.1109/TMIT.2006.871360>
15. Chu, Q.-X., Yan, J.-M.: A two-layer planar spatial power divider/combiner. In: IEEE Int. Microw. Symp. Digest, pp. 989–992 (2009). <https://doi.org/10.1109/MWSYM.2009.5165865>
16. Ghavidel, A., Khierdoost, A.: Broadband millimeter wave planar power combiner/divider. Int. Symp. Networks Comput. Comm, 1–4. (2019). <https://doi.org/10.1109/ISNCC.2019.8909088>
17. Agah, A., et al.: Active millimeter-wave phase-shift Doherty power amplifier in 45-nm SOI CMOS. IEEE J. Solid-state Circuits. 48(10), 2338–2350 (2013). <https://doi.org/10.1109/JSSC.2013.2269854>
18. Doherty, W.H.: A new high efficiency power amplifier for modulated waves. Proc. IRE. 24(9), 1163–1182 (1936). <https://doi.org/10.1109/JRPROC.1936.228468>
19. Wang, H., et al.: Towards energy-efficient 5G mm-wave links: exploiting broadband mm-wave Doherty power amplifier and multi-feed antenna with direct on antenna power combining. In: IEEE Bipolar/BiCMOS Circuits and Technology Meeting, pp. 30–37Miami (2017). <https://doi.org/10.1109/BCTM.2017.8112905>

20. Mortazavi, M., et al.: A 30GHz 4-way series Doherty digital polar transmitter achieving 18% drain efficiency and -27.6dB EVM while transmitting 300MHz 64-QAM OFDM signal. In: IEEE Custom Integrated Circuits Conference (2021). <https://doi.org/10.1109/CICC51472.2021>
21. Roev, A., et al.: A wideband and low-loss spatial power combining module for mm-wave high-power amplifiers. IEEE Access 8, 194858–194867 (2020). <https://doi.org/10.1109/ACCESS.2020.3033623>
22. Razavi, B.: RF microelectronics. Prentice Hall (2012)
23. Cavallo, D., Syed, W.H., Neto, A.: Closed-form analysis of artificial dielectric layers—Part II: extension to multiple layers and arbitrary illumination. IEEE Trans. Antennas Propag. 62(12), 6265–6273 (2014). <https://doi.org/10.1109/TAP.2014.2365236>
24. Cavallo, D., Felita, C.: Analytical formulas for artificial dielectrics with nonaligned layers. IEEE Trans. Antennas Propag. 65(10), 5303–5311 (2017). <https://doi.org/10.1109/TAP.2017.2738064>
25. Syed, W.H., et al.: Design, fabrication, and measurements of a 0.3 THz on-chip double slot antenna enhanced by artificial dielectrics. IEEE Trans. Thz Sci. Techn. 5(2), 288–298 (2015). <https://doi.org/10.1109/THZ.2015.2399276>
26. Neo, W.C.E., et al.: A mixed-signal approach towards linear and efficient N-way Doherty amplifiers. IEEE Trans. Microw. Theor. Techn. 55(5), 866–879 (2007). <https://doi.org/10.1109/TMTT.2007.895160>
27. Rogers corporation: Copper foils for high frequency materials. <http://payalnik.com.ua/upload/docum/Copper-Foils-for-High-Frequency-Circuit-Materials.pdf>

How to cite this article: van Schelven, R.M., Spirito, M., Cavallo, D. Efficient waveguide power combiners at mm-wave frequencies. IET Microw. Antennas Propag. 1–11 (2023). <https://doi.org/10.1049/mia2.12349>

APPENDIX

Model of power amplifiers as sources

It is convenient to represent the PA, schematically shown in Figure A1a, as a Norton equivalent source. The resulting circuit is depicted in Figure A1b, where the PA is represented as a voltage controlled current source. The control voltage signal v_{in} determines the value of the current and generator impedance. The PAs under consideration consist of multiple sub-PAs which are connected in parallel, that can be either on or off, according to the simplified circuit representation shown in Figure A1c. The signal v_{in} controls the number of sub-PAs that are switched on (N_{on}). Each active sub-PA can also be represented as a Norton equivalent source with current generator I_{sub} and internal resistance R_{sub} , assumed to be $2k\Omega$. On the contrary, the inactive sub-PAs are ideally open circuits. We assume that the PA is designed such that the parasitics can be represented as a single resistor, $R_{par} = 480\Omega$, thus capacitive and inductive effects are neglected.

Therefore, the current $I_{PA}(v_{in})$ can be expressed as $I_{PA} = I_{sub} N_{on}$, while the impedance $Z_{PA}(v_{in}) = R_{par} || (R_{sub} / N_{on})$. The control voltage v_{in} is assumed to be linearly proportional to N_{on} and normalised so that $v_{in} = 0$ corresponds to all sub-PAs switched off and $v_{in} = 1$ refers to all sub-PAs being

on. The resulting current and impedance of the Norton generator are shown in Figure A2.

If we assume PAs operating as class B, the total power supplied to the PA is given by [22]:

$$P_{supply} = V_{DD} \frac{2}{\pi} |I_{out}| \quad (A1)$$

where V_{DD} is the drain voltage of the transistor (Figure A1c) and I_{out} is the output voltage of the PA. The output power is

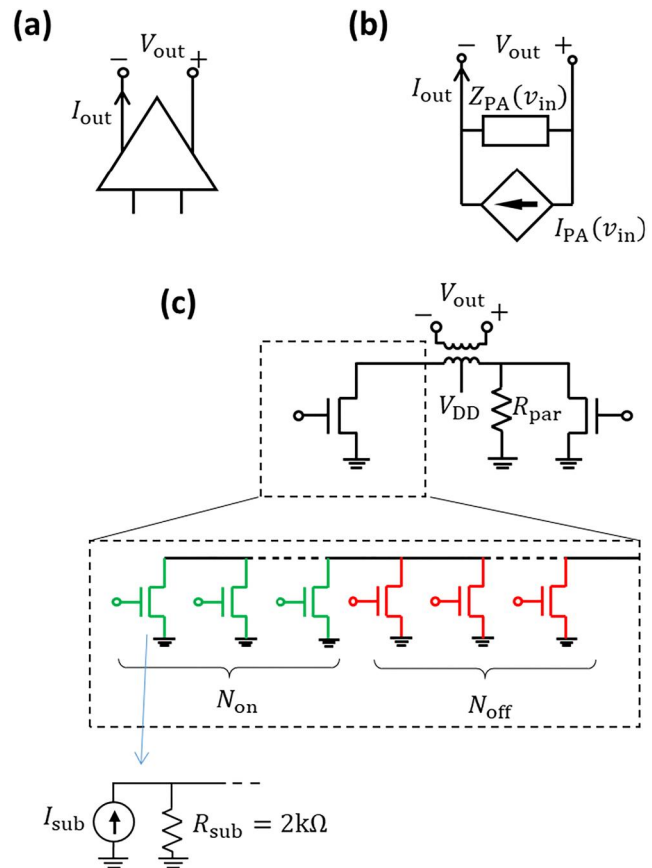


FIGURE A1 (a) Circuit representation of a power amplifier (PA) consisting of multiple sub-PAs. (b) Norton-equivalent circuit of the PA. (c) Schematic drawing of a PA consisting of multiple sub-PAs.

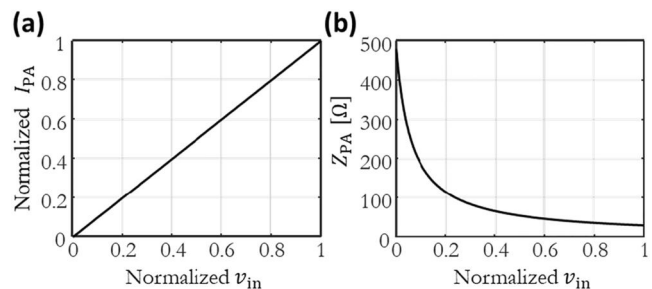


FIGURE A2 (a) Normalised current and (b) internal impedance of the Norton generator, as a function of v_{in} .

$$P_{\text{out}} = \frac{1}{2} |V_{\text{out}}|^2 \operatorname{Re} \left\{ \frac{1}{Z_{\text{out}}} \right\} \quad (\text{A2})$$

where V_{out} is the output voltage of the PA and $Z_{\text{out}} = V_{\text{out}}/I_{\text{out}}$. The efficiency of a class B PA can be found as the ratio between P_{out} and P_{supply} that, for real output impedance, gives

$$\eta = \frac{\pi}{4} \frac{|V_{\text{out}}|}{V_{\text{DD}}} \quad (\text{A3})$$

Since $|V_{\text{out}}|$ cannot exceed V_{DD} , the maximum efficiency of a class B PA is $\eta_{\text{max}} = \pi/4 \approx 79\%$ and is reached when $|V_{\text{out}}| = V_{\text{DD}}$. If a certain frequency range is considered, since

the output voltages of the PAs cannot exceed the supply voltage, the condition

$$|V_{\text{out}}| \leq V_{\text{DD}} \quad (\text{A4})$$

can be imposed for every frequency and for the full range of output current. In practice, this can be realised by tuning the maximum value for control signal v_{in} at different frequencies. This results in a changing number of sub-PAs being switched on for different frequencies, and therefore in a frequency dependent port impedance Z_{PA} .